Three-Dimensional Multilayered Nanostructures with Controlled Orientation of Microdomains from Cross-Linkable Block Copolymers

Hyunjung Jung,[†,¶] Dongjune Hwang,[†,¶] Eunhye Kim,[‡] Byung-Jae Kim,[†] Won Bo Lee,[§] Justin E. Poelma,[⊥] Jihyun Kim,[†] Craig J. Hawker,[⊥] June Huh,[∥] Du Yeol Ryu,[‡,*] and Joona Bang[†,*]

[†]Department of Chemical and Biological Engineering, Korea University, Seoul 136-701, Republic of Korea, [‡]Department of Chemical and Biomolecular Engineering, Yonsei University, Seoul 120-749, Republic of Korea, [§]Department of Chemical and Biomolecular Engineering, Sogang University, Seoul 121-742, Republic of Korea, [⊥]Departments of Materials, Chemistry and Biochemistry and Materials Research Laboratory, University of California, Santa Barbara, California 93106, United States, and [∥]Department of Materials Science and Engineering, Yonsei University, Seoul 120-749, Republic of Korea. [¶]These authors contributed equally to this work.

ABSTRACT Three-dimensional (3D) nanostructures were obtained by the directed formation of multilayer block copolymer (BCP) thin films. The initial step in this strategy involves the assembly and cross-linking of cylinder-forming polystyrene-*b*-poly(methyl methacrylate) (PS-*b*-PMMA) BCP, in which 1.5 mol % of reactive azido ($-N_3$) groups were randomly incorporated along the styrene backbone. Significantly, assembly of thin films of lamellar-forming BCPs on top of the underlying cross-linked cylindrical layer exhibited perpendicular orientations of microdomains between lamellae and cylinder layers. From the theoretical calculation of free energy in the multilayers, it was found that the nematic interactions between polymer chains at the interface play a critical role in the perpendicular orientation of lamellae on the cross-linked cylinder layers. Removal of the PMMA domains then affords nonsymmetrical nanostructures which illustrate the promise of this strategy for the design of well-defined 3D nanotemplates. It was also demonstrated that this structure can be effectively used to enhance the light extraction efficiency of GaN light-emitting diodes. Furthermore, we anticipate that such 3D nanotemplates can be applied to various areas, including advanced BCP nanolithography and responsive surface coating.

KEYWORDS: block copolymer thin film · multilayer · 3D nanostructure · light extraction efficiency · GRIN layer

Nanostructured patterns obtained from the self-assembly of block copolymers (BCPs) have been extensively studied from a scientific perspective as well as in various applications such as nanolithography, microelectronics, nanoreactors for nanoparticle/nanowire fabrication, separation membranes, among others.[1−7] From the scientific viewpoint, the fundamental physics of BCPs in bulk and in thin films have been well-established,[1−4] and significant effort is now being directed toward industrial applications such as the AirGap technology from IBM.[8] For most applications of BCP thin films, controlling the desired orientation and lateral ordering of microdomains has been the critical issue, and subsequently, many methodologies have been developed.

While significant effort has been devoted to controlling two-dimensional (2D) organization of BCP films (*i.e.*, lamellar or cylindrical microdomains), a future challenge for BCP lithography is the fabrication of more complex, three-dimensional (3D) scaffolds. In this case, it is a prerequisite that precise control of microdomains between various nanostructures should be accomplished. As preceding examples, Nealey and coworkers have employed the chemically patterned surfaces having a similar length scale as BCP to improve the lateral ordering of BCP microdomains.[9−13] By controlling the pattern size and the surface chemistry, they demonstrated that BCP microdomains are well registered with the underlying patterns and thus the lateral ordering of microdomains can be perfectly controlled over large areas. The underlying patterns were not limited to the simple line or dot patterns, and various nonregular shapes such as jogs, T-junctions, and isolated patterns were successfully applied.[11,12] In this case, blends of BCP and homopolymers were used so that the free energy cost by chain stretching of BCP at high curvature areas can be compensated by homopolymers. Furthermore, sparse patterns have been recently employed to direct the lateral ordering of BCP microdomains.[13,14] For sparse surface patterns in which the pattern sizes are greater than that of BCP by a factor of 2 or 4, BCP microdomains were perfectly ordered with their natural domain spacing. In addition, it was also shown that several defects in the

* Address correspondence to joona@korea.ac.kr, dyryu@yonsei.ac.kr.

Received for review February 21, 2011 and accepted July 13, 2011.

Published online July 13, 2011
10.1021/nn2006943

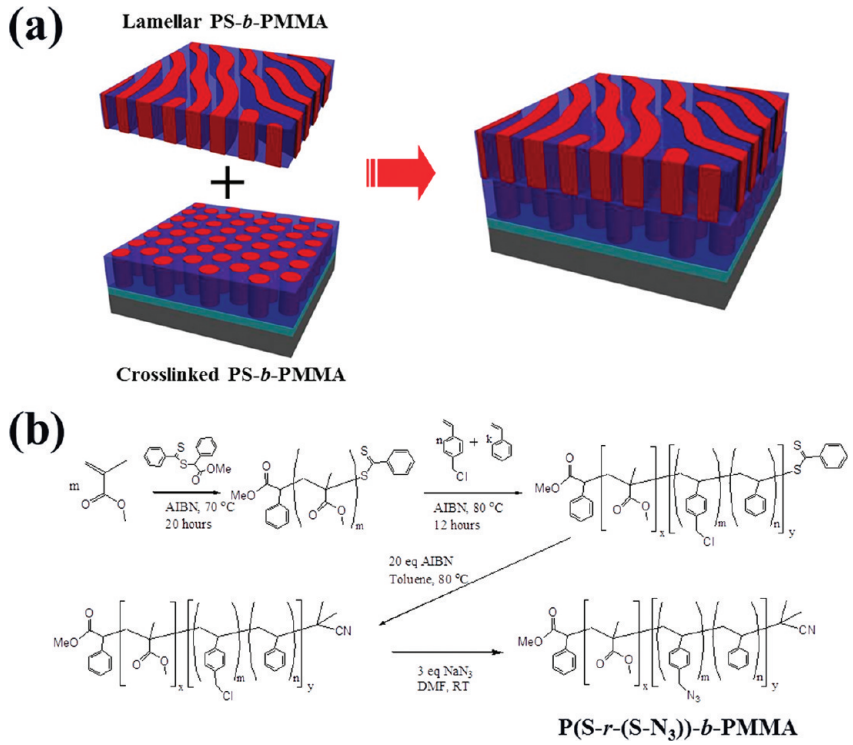

Figure 1. (a) Schematic illustration for the fabrication of BCP multilayers. (b) Synthesis of cross-linkable P(S-*r*-S-N_3)-*b*-PMMA BCP.

surface patterns can be significantly rectified by the self-assembly of BCPs. These results imply that the surface patterns do not need to be an exact replica of overlaying BCP microdomains, thereby providing a possible route for more complicated 3D BCP nanostructures.

However, the generation of 3D nanostructures is still a challenge and there have been only a few examples on the fabrication of 3D scaffolds. Daoulas *et al.* have recently demonstrated that complex 3D structures can be formed when a blend of lamellar-forming BCP, polystyrene-*b*-poly(methyl methacrylate) (PS-*b*-PMMA), and its respective homopolymers were self-assembled on chemically patterned square arrays.[15] In this case, quadratically perforated lamellae or bicontinuous morphologies can be stabilized depending on the pattern dimensions and film thickness. Alternatively, 3D multilayered structures can be prepared through layer-by-layer stacking[16,17] *via* cross-linking BCP layers which allows each layer to be sequentially prepared without perturbing the underlying layers. This strategy was first proposed by Ruiz and co-workers.[18] They fabricated the bilayered BCP films consisting of a top lamellar PS-*b*-PMMA layer and horizontally oriented PS-*b*-PMMA cylinders as underlying layers. In this case, PS block in PS-*b*-PMMA cylinders was cross-linked by UV light, and subsequently, the lamellar forming PS-*b*-PMMA BCP was deposited. Then, it was shown that the top lamellar BCP microdomains follow the underlying cylinder patterns, similar to the case of a chemically patterned surface. Very recently, a similar approach was used to fabricate more complicated 3D multilayered nanostructures consisting of lamellar and cylindrical BCP films.[19] During the stacking process, each BCP layer was separated by sputtering porous and dense silicon membranes, and hence the orientation of each BCP microdomain was independently controlled. On the other hand, if the cross-linkable BCPs were designed, more robust and well-defined multilayered scaffolds can be readily prepared by facile cross-linking reactions with a simpler process. Using this strategy, we have previously demonstrated high fidelity registration in a multilayer film fabricated from an initial cylindrical microdomain based on PS-*b*-PMMA BCP containing cross-linkable benzocyclobutene (BCB) units followed by a second layer of PS-*b*-PMMA cylinders.[17]

In this work, complex 3D multilayered nanostructures based on different morphologies (cylinder and lamella) are fabricated using cross-linkable BCPs. As illustrated in Figure 1a, it was found that formation of lamellar microdomains on top of a cross-linked cylindrical layer leads to a perpendicular orientation relative to the film surface. The resulting 3D multilayered nanostructures were carefully investigated using scanning force microscopy (SFM), grazing-incidence small-angle X-ray scattering (GISAXS), scanning electron microscopy (SEM), and transmission electron microscopy (TEM). We also theoretically considered the free energy of multilayered structures, and it was found that the perpendicular orientation of lamellae on the cross-linked

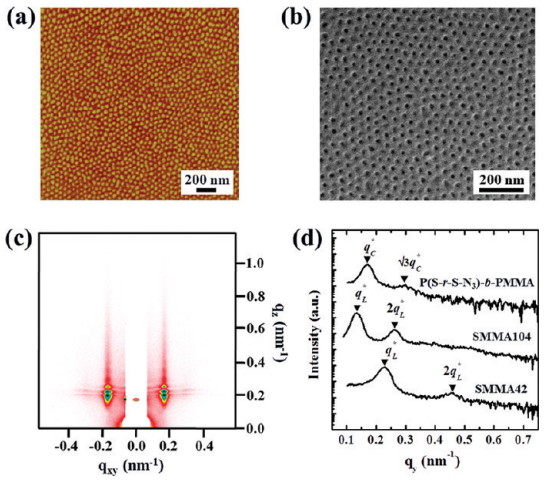

Figure 2. (a) SFM phase image and (b) SEM image of cylinder-forming cross-linked P(S-*r*-S-N_3)-*b*-PMMA thin film. (b) PMMA block was removed by UV irradiation. (c) Two-dimensional GISAXS patterns at incident angles of 0.18° for cylinder-forming cross-linked P(S-*r*-S-N_3)-*b*-PMMA thin film. (d) Intensity profiles scanned at constant $q_z = 0.285$ nm^{-1} for 2D GISAXS patterns of P(S-*r*-S-N_3)-*b*-PMMA, SMMA104, and SMMA42 thin films. See the Supporting Information for the 2D GISAXS patterns for SMMA104 and SMMA42 (Figure S2).

cylindrical layer was mainly due to the nematic interaction at the interface. Furthermore, it was demonstrated that such structures can be used to improve the light extraction efficiency in GaN light-emitting diodes (LEDs) by forming a graded refractive index (GRIN) layer on the GaN surfaces.

RESULTS AND DISCUSSION

Key to these studies was the synthesis of cross-linkable PS-*b*-PMMA BCPs, which were prepared by reversible addition−fragmentation chain transfer (RAFT) polymerization.[17,20] Previously, it has been demonstrated that copolymers containing azido (−N_3) groups along the backbone can be effectively cross-linked through either thermal or UV treatment.[21] In this work, the design of the cross-linkable PS-*b*-PMMA copolymers includes the incorporation of small amounts of the azide repeat unit in the PS block (Figure 1b), where the functional azide units in the PS block component are integrated into inter- or intramolecular linkages at higher temperature. The resulting cross-linkable PS-*b*-PMMA BCP, denoted P(S-*r*-S-N_3)-*b*-PMMA, contains 1.5 mol % of azide unit relative to styrene with the overall weight average molecular weight (M_w) and polydispersity index (PDI) being 69 000 g/mol and 1.20, respectively (Supporting Information, Figure S1). The volume fraction of the PMMA block in P(S-*r*-S-N_3)-*b*-PMMA was controlled to be ~0.27 in order to obtain a cylindrical microdomain morphology. Cross-linkable BCP films were then prepared by spin-coating toluene solutions of P(S-*r*-S-N_3)-*b*-PMMA (1 wt %) onto silicon substrates to yield a film thickness of ~50 nm. Note that all silicon surfaces used in this study were neutralized with PS-*r*-PMMA random copolymers before spin coating.[21−25] Initial alignment of these films was achieved by annealing at 160 °C for 24 h to allow chain mobility above the glass transition temperatures (T_g) of both PS (100 °C) and PMMA (115 °C), leading to vertical cylindrical microdomains. Significantly, the annealing temperature of 160 °C was chosen to be below the cross-linking temperature, which allows microdomain orientation to occur prior to any cross-linking.[17] After thermal annealing and alignment, the films were cross-linked at 250 °C for 1 h under vacuum,[17,21] resulting in a stable underlying layer composed of the perpendicular cylinder arrays. It should be pointed out that the random cross-linking reaction only at the PS block component is enough to ensure the dimensional stability and insolubility for further solution processes.[17,20]

Figure 2 shows a scanning force microscopy (SFM) phase image and scanning electron microscopy (SEM) image for BCP films and the corresponding two-dimensional grazing-incidence small-angle X-ray scattering (GISAXS) patterns. In the scattering geometry, q_{xy} is the scattering vector normal to the plane of incidence (parallel to the film surface), where the domain spacing is determined by L_o (or C_o) = $2\pi/q_{xy}$*, where L_o and C_o correspond to the domain spacing of lamellae or cylinders, respectively; q_z is the scattering vector normal to the sample surface, defined as $q_z = (4\pi/\lambda)\sin\theta$, where λ is the wavelength of the X-rays and 2θ is the scattering angle. The incident angle was set at 0.18°, which is above the critical angle (0.135°) for PS-*b*-PMMA thin films. The SFM and SEM images of the cross-linked BCP film of P(S-*r*-S-N_3)-*b*-PMMA, as shown in Figure 2a,b, indicate that the cylindrical microdomains after cross-linking were oriented normal to the film surface, which was further confirmed by sharp Bragg rods at q_{xy}* = 0.165 nm^{-1} along q_z. The domain spacing and diameter of this film is 38.1 nm from GISAXS and 22.3 nm from SFM measurements, respectively. It should be noted that there was no significant change in the domain spacing or diameter of the cylindrical microdomain upon cross-linking reaction, which is due to the relatively small amount of cross-linkable azide units incorporated (1.5 mol % relative to styrene). After cross-linking, the resulting films are insoluble,[17,20] which allows the next layer to be readily fabricated on top of the cross-linked film to produce the desired multilayered nanostructure.

When the directed registration of different morphologies was examined, two lamellar-forming PS-*b*-PMMA BCPs having number-average molecular weights of 104.0 and 42.0 kg/mol were employed, denoted as SMMA104 and SMMA42, respectively. On the neutral surfaces, thin films of SMMA104 and SMMA42 show a perpendicular orientation of lamellae as evidenced by the "fingerprint" patterns in SFM images after annealing at 190 °C for 24 h (Supporting Information, Figure S2).

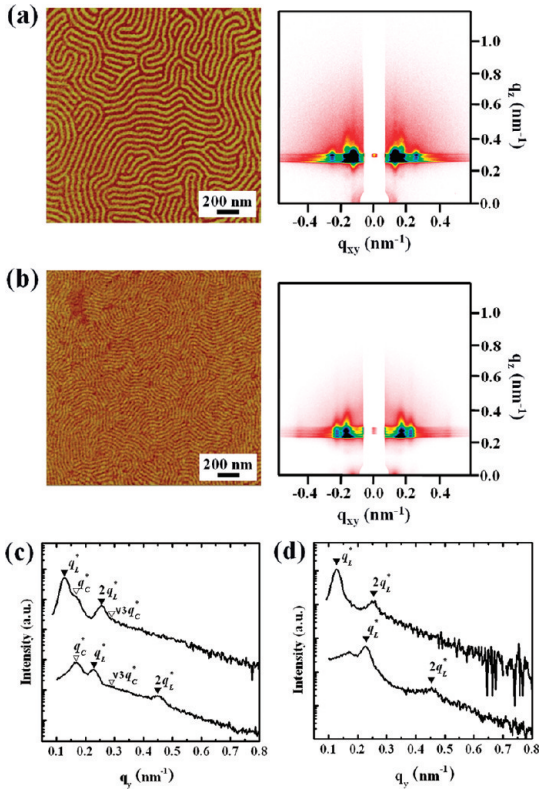

Figure 3. SFM phase images and the corresponding 2D GISAXS patterns at incident angles of 0.18° for (a) SMMA104/cylinder multilayers and (b) SMMA42/cylinder multilayers. (c) Intensity profiles scanned at constant q_z = 0.285 nm^{-1} for 2D GISAXS patterns in (a) and (b). (d) Intensity profiles scanned at constant q_z = 0.158 nm^{-1} for 2D GISAXS patterns obtained at incident angle of 0.10°. See the Supporting Information for the 2D GISAXS patterns (Figure S3). (c,d) Top and bottom curves correspond to SMMA104/cylinder and SMMA42/cylinder multilayers, respectively.

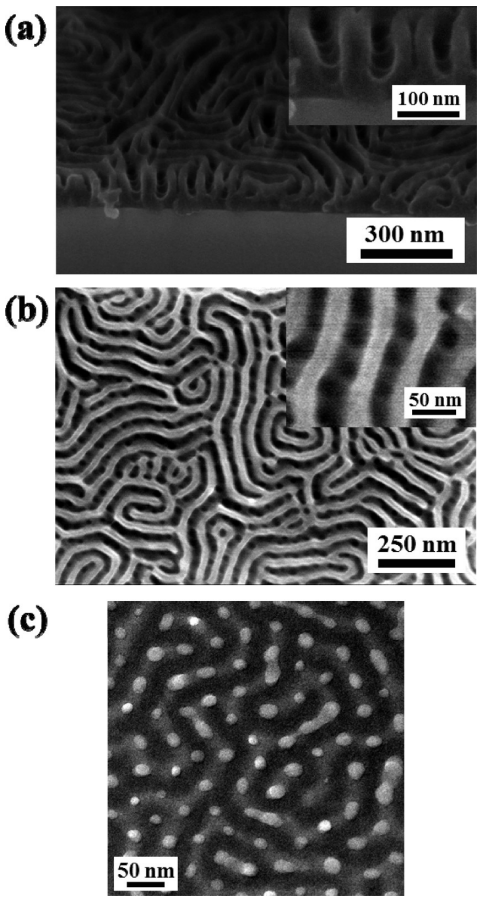

Figure 4. (a) Tilted- and (b) top-view of SEM images for SMMA104/cylinder multilayers after removing the PMMA block by UV irradiation. (c) Top-view of TEM images for SMMA104/cylinder multilayers after removing the PMMA block by UV irradiation.

According to in-plane scattering analysis taken at q_z = 0.285 nm^{-1} (Figure 2d), the domain spacing of SMMA104 and SMMA42 is 47.6 and 27.8 nm, respectively. Assuming that the chain stretching is similar in PS and PMMA blocks, the thickness of the PMMA domain for SMMA104 and SMMA42 is 23.8 and 13.9 nm, respectively. Consequently, the diameter of cylinders in P(S-*r*-S-N_3)-*b*-PMMA is similar to the size of the PMMA lamellae in SMMA104 and much larger than that in SMMA42.

Thin films of PS-*b*-PMMA lamellae were then spin-coated on cross-linked P(S-*r*-S-N_3)-*b*-PMMA films with the underlying cylindrical microdomains oriented normal to the film surface. The film thickness was controlled to be less than $2L_o$ (interlamellar distance or domain spacing) of BCPs, taken as 65 and 45 nm for SMMA104 and SMMA42 BCPs, respectively. Figure 3 shows the thin film morphology of PS-*b*-PMMA lamellae on the cross-linked P(S-*r*-S-N_3)-*b*-PMMA layers after thermal annealing at 190 °C for 24 h. In this case, the SFM images indicate that both SMMA104 and SMMA42 lamellae are oriented perpendicular to the film surfaces. The GISAXS measurements were performed at incident angles of 0.10 and 0.18°, which is below and above the critical angle (0.135°) of the porous PS-*b*-PMMA films, respectively. To increase the X-ray contrast of films, the PMMA microdomains were removed by UV irradiation followed by rinsing with acetic acid, resulting in nanoporous films.[17,26−28] The GISAXS patterns in Figure 3a,b were obtained at the incident angle of 0.18°, and thus the X-ray beam penetrates the entire films, reflecting the features of a combination of (top) lamellae and (bottom) cylinder layers. In these patterns, the Bragg rods can be clearly seen, indicating that both cylindrical and lamellar microdomains in multilayers are oriented normal to the substrates. The first-order peaks at q_{xy} = 0.132 nm^{-1} in Figure 3a and 0.226 nm^{-1} in Figure 3b arise from top lamellae layer, while the peak at q_{xy} = 0.165 nm^{-1} in both patterns corresponds to the first-order reflection of the underlying cylinder layer. These peaks can be clearly distinguished in the intensity profiles scanned at q_z = 0.285 nm^{-1} as a function of q_{xy} (Figure 3c). It should also be noted that the domain spacings of cylinders and lamellae films remain unchanged compared to

those of single layers. When the incident angle is 0.10°, which is below the critical angle of the films, only reflections from the top lamellae layers were observed (Figure 3d; see also Supporting Information, Figure S3). However, there is a small peak at $q_{xy} = 0.165$ nm^{-1} in the scattering pattern of the SMMA42/cylinder multilayer, which is apparently the first-order peak from the underlying cylindrical layer. In fact, we observed that a significant percentage of lamellae for the lower molecular weight SMMA42 diblock collapsed after removal of PMMA block (Supporting Information, Figure S4). As a result, the underlying cylindrical layers were exposed to the X-ray beam even at the incident angle of 0.10°.

The internal structure of multilayers was further investigated by SEM after removing the PMMA blocks by UV irradiation and acetic acid treatments to enhance the contrast between PS and PMMA block components for SEM. From the tilted- and top-view of SEM images in Figure 4a,b, a distinct multilayer structure can be observed which consists of an upper lamellar layer and an underlying cylindrical layer. The perpendicular orientation of the lamellar and cylindrical microdomains is also readily apparent and is consistent with the GISAXS patterns. Of particular note is the observation of cylindrical pores between PS lamellae, which strongly implies that the PMMA cylinders in the underlying layers have a high degree of registration with the PMMA lamellae in the upper layer. This is confirmed by the top-view of transmission electron microscopy (TEM) image in Figure 4c, where brighter spots and lines corresponding to the PMMA cylinders and lamellae, respectively (PMMA blocks have been removed), are observed. As with the SEM images, it is apparent that the majority of PMMA cylinders (bright spots) are coincident with the PMMA lamellae (bright lines). From the image analysis of Figure 4c, we estimated the center-to-center distance, and it ranges from 38.7 to 54.2 nm. Also, we compared these values with those from the single-layer SEM image in Figure 2b. In this case, the center-to-center distance ranges from 38.7 to 49.5 nm, suggesting that the center-to-center distance of cylinders from the bilayer exhibits broader distribution than that from the single layer, although the average center-to-center distance remains unchanged. We attribute this behavior to the consequence of minimizing wetting energy at the interlayer boundary in the cylinder/lamellar bilayer where the two intrinsic length scales of domain spacing slightly differ. It is worth pointing out that both cross-linked cylinders and the lamellar film can adjust their domain spacing to minimize wetting energy. Of course, adjusting their domain spacing from their bulk values results in elastic penalties. However, when both length scales are similar (or close to commensurate conditions), such elastic penalty is overcome by minimized wetting energies. As described in the theoretical calculation in Methods, we considered the elastic energy in calculating the free energy of our multilayer structures.

These results are also noteworthy as they suggest that the heterogeneous surface of a vertically aligned cylindrical BCP film is effective in controlling the orientation of BCP microdomains. However, a fundamental difference exists between the surfaces of a BCP film and a random copolymer layer. The neutral surface formed from a PS-*r*-PMMA random copolymer is chemically homogeneous, which provides balanced interactions on the surface toward PS and PMMA. As a result, the orientation is determined mainly by entropy differences between perpendicular and parallel orientations.[21−25] In contrast, the surface of a vertically aligned cylindrical BCP film is chemically heterogeneous on the same length scales due to the distribution of distinct BCP microdomains. Therefore, the perpendicular orientation of PS-*b*-PMMA lamellae in the above multilayer systems cannot be explained in the same way as for a random copolymer neutral surface. Alternatively, the situation is similar to the case where a patterned surface (lamellae) is commensurate with the PS-*b*-PMMA lamellae. In that case, surface-induced density fluctuations promote a perpendicular orientation.[29] Since our patterned surface is not lamellae but hexagonal cylinders, there is a wetting energy difference between both orientations that favors parallel alignment. The system therefore minimizes the wetting energy at the interface of cylinders/lamellae layers, as shown in Figure 4, where the PMMA microdomains in the respective layers of the bilayer film have a high degree of registration due to maximization of PMMA−PMMA interfacial area. In order to understand the difference in wetting energy, the fraction of unfavorable interaction area in the case of parallel and perpendicular orientations was evaluated. From TEM image analysis, the fraction was estimated as ∼0.37 for the perpendicular orientation of lamellae in the multilayer. If the lamellae show a parallel orientation in the multilayer, the PS block will interact with the underlying layer, and if we assume that the fraction of PMMA microdomains on the film surface is the same as the volume fraction, 0.27, then the PMMA microdomains interact with 27% of PS block. From these values, it is clearly not a wetting energy difference that leads to a stable perpendicular orientation. Consequently, the wetting energy at the interface is not solely responsible for the perpendicular orientation of lamellae in the multilayers, though the registration of microdomains does certainly minimize the wetting energy. These results suggest that other factors synergistically contribute to the perpendicular orientation and registration of the microdomains.

A highly plausible factor is concerned with an entropy-type attraction, namely, "*nematic interaction*" between a chain molecule and a flat surface. In analogy with liquid crystal, this interaction originates from

the surface preferring chain segments to lie along the surface. Since the chains are oriented along the surface in the perpendicular lamellae ($L_\perp$), there is a nematic interaction at the film boundary which favors $L_\perp$. On the other hand, such entropy-type attraction is absent in parallel lamellae ($L_\parallel$) where chains are oriented normal to the surface. According to the theory developed by Pickett,[30] the nematic interaction in terms of the interfacial tension is given as $\gamma_n \approx -k_BT(a/V)(h/R_\perp)^2$, where γ_n is the interfacial tension due to the nematic interaction, k_BT is the thermal energy, a is the packing length of chain, V is the displaced volume per chain in the melt, $h = L_o/4$ with interlamellar spacing L_o, and $R_\perp$ is the end-to-end distance of a chain in the direction perpendicular to the surface ($R_\perp = (V/2a)^{1/2}$). It is also important to realize that the magnitude of γ_n scales as $\sim N^{-2/3}$, where N is the chain length, which suggests that the nematic attraction becomes more pronounced for a smaller chain. Using the parameters available for SMMA104 and SMMA42, the interfacial tensions due to nematic interaction at 190 °C are estimated as $\gamma_n \approx -0.19$ dyn/cm for SMMA104 (using $a \approx 1$ nm, $V \approx 100$ nm^3, $h/R_\perp \approx 1.7$) and $\gamma_n \approx -0.36$ dyn/cm for SMMA42 (using $a \approx 1$ nm, $V \approx 40$ nm^3, $h/R_\perp = 1.5$). Having estimated the magnitude of γ_n, we can infer the stability of $L_\perp$ for each case of SMMA104 and SMMA42 in terms of the interfacial free energy. The interfacial free energy $F_{s,\perp}$ between $L_\perp$ and the cross-linked cylinder layer is given by $F_{s,\perp}/S = \Psi\gamma_{AB} + \gamma_n$, where S is the lamellae/cylinder interfacial area, γ_{AB} is the A/B interfacial tension (let A and B denote PMMA and PS, respectively), and Ψ is the areal fraction of A/B interlayer contacts (either cylinder A/lamellar B or lamellar A/cylinder B contacts) relative to the total area S. This should be compared with the interfacial free energy for $L_\parallel$ given as $F_{s\parallel}/S = g\gamma_{AB}$, where g is the fraction of minor A block (PMMA) in the cross-linked cylinder layer. Therefore, we can deduce an inequality for the stability of $L_\perp$: $\Delta_s = F_{s\parallel}/S\gamma_{AB} - F_{s,\perp}/S\gamma_{AB} = g - \Psi - \gamma_n/\gamma_{AB} > 0$. The areal fraction Ψ can be also theoretically determined by a model based on strong segregation theory combined a network model (see theoretical calculation in Methods). For the SMMA104 system, where the intrinsic interlamellar spacing L_o is 47.6 nm on the cylinder layer with the cylinder-to-cylinder distance of $C_o \cong 44$ nm, we theoretically find $\Psi = 0.35$, which is in good agreement with the experimental value for the areal fraction $\Psi_{exp} \cong 0.37$. This leads to $\Delta_s = 0.093$ given that $g = 0.27$, $\Psi = 0.35$, $\gamma_n = -0.19$ dyn/cm, and $\gamma_{AB} = 1.1$ dyn/cm at 190 °C. In the case of SMMA42 ($C_o \cong 44$ nm and $L_o = 27.8$ nm), on the other hand, we find that $\Psi = 0.41$ and $\Delta_s = 0.22$. Despite $g < \Psi$ for both cases, the positive values of Δ_s for both SMMA104 and SMMA42 reveal that the nematic interaction plays a critical role for the lamellar orientation and rationalizes the perpendicular lamellar orientations as observed in the experimental results.

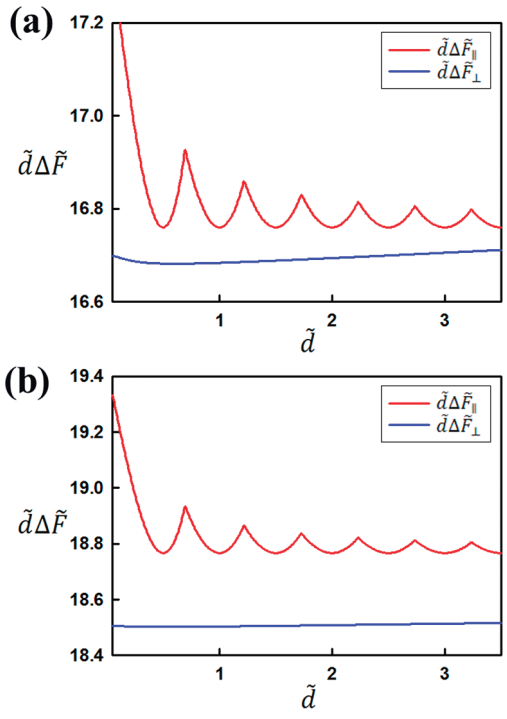

Figure 5. Free energy change per unit area ($\propto d\Delta F$) for parallel ($\parallel$) and perpendicular ($\perp$) orientation as a function of the film thickness d of lamellar layer for (a) SMMA104 and for (b) SMMA42.

The importance of this entropy-originated, nematic interaction is basically due to the rather weak PS/PMMA interfacial tension (γ_{AB}) such that γ_n/γ_{AB} gives a nontrivial contribution to the difference in interfacial free energy Δ_s. For a block copolymer with high γ_{AB} such as polystyrene-*b*-poly(4-vinyl pyridine), however, the nematic contribution would be negligible because $\gamma_n/\gamma_{AB} \ll 1$. In such case, the criteria for stable $L_\perp$ is determined almost solely by the difference in wetting energy: $\Delta_s = g - \Psi > 0$. Similar entropic domination in the interfacial tension has also been reported in the thin films of polystyrene-*b*-polybutadiene (PS-*b*-PB) on silicon wafer, where the Si/SiO_x substrate is nearly nonselective to both blocks.[31] In addition to nematic interaction, it should also be mentioned that there is another possibility of entropy-originated interactions arising from the depletion of polymer density in the vicinity of the surface.[32−35] The density depletion near the surface gives rise to a local decrease in either surface tension or interfacial tension at the A/B interface, which can also lead to an effective interaction of surface favoring $L_\perp$ over $L_\parallel$. Such entropy-type interactions, either by nematic effect or by density depletion, can encourage the formation of $L_\perp$. In addition, it is also worth noting that some other factors such as substrate roughness may play roles.[36,37]

The total free energy in this system, including aforementioned interfacial free energy, can be described as $\Delta F = (1 - \phi)\Delta F_{CCL} + \phi\Delta F_{lam}$, where ΔF_{CCL} is the elastic energy change of CCL from its undeformed state, ΔF_{lam}

is the free energy change of a lamellar film on CCL (deviated from the bulk free energy $F_{lam,o}$) and ϕ is the volume fraction of a lamellar film in the whole layer (lamellar film and CCL). The formulas and theoretical terms including the nematic interaction are documented in the theoretical calculation in Methods. Figure 5 presents the free energy change per unit area of $L_\perp$ and $L_\parallel$ on the cross-linked cylinder layer as a function of the film thickness d of lamellar layer for SMMA 104 and SMMA42, respectively. For both cases, the free energy of $L_\perp$ is lower than that of $L_\parallel$ over the whole film thickness range considered, which theoretically supports that $L_\perp$ is stable over $L_\parallel$ in our system.

From a practical viewpoint, it can be anticipated that such 3D nanostructures can be used in various applications including advanced BCP nanolithography, efficient surface coating, and scaffolds for complex nanostructures. As one example, we fabricated 3D multilayered structures on the surface of GaN-based light-emitting diodes (LEDs) to enhance the light extraction efficiency.[38] The low light extraction efficiency in GaN-based LEDs has been an issue due to the large difference in refractive index (n) between GaN ($n = 2.5$) and air ($n = 1$), which results in wave-guiding. However, the light output can be enhanced by inserting a thin layer (*i.e.*, anti-reflective layer), with a refractive index between GaN and air. Recently, it has been reported that a graded refractive index (GRIN) layer can further improve light extraction efficiency by gradually tailoring the refractive index from the substrate to the air. Compared to the single-layer coating, it is well-established that the gradual change of the refractive index in a GRIN layer can further reduce the reflectance at the interface due to the suppression of the Fresnel reflection, $R = [(n_1 - n_2)/(n_1 + n_2)]^2$, where R is the reflection coefficient and n_1 and n_2 are the refractive indices of each material. Note that this equation is for the case when the incident light is nearly normal to the interface. According to this equation, it can be seen that the reflection loss of the double layer should be lower due to the gradual change in the refractive index. As another advantage of a GRIN layer, it was suggested that a GRIN layer can yield omnidirectional, broad-band anti-reflection features, while the single-layer works only at a single wavelength and at normal incidence.[39] Therefore, overall performances of anti-reflective coating are much better for the GRIN layer than single layers. Although GRIN layers were effective in improving light output in GaN-based LEDs, the fabrication of GRIN layers is complicated and requires expensive vacuum procedures.[40,41] For example, most efforts have been on the deposition of inorganic materials, such as ITO or titanium oxide[40,41] *via* a relatively complicated vacuum process. Although such GRIN layers could also be fabricated by a solution process of organic materials, there are not many examples so far. Very recently, we reported that a GRIN layer

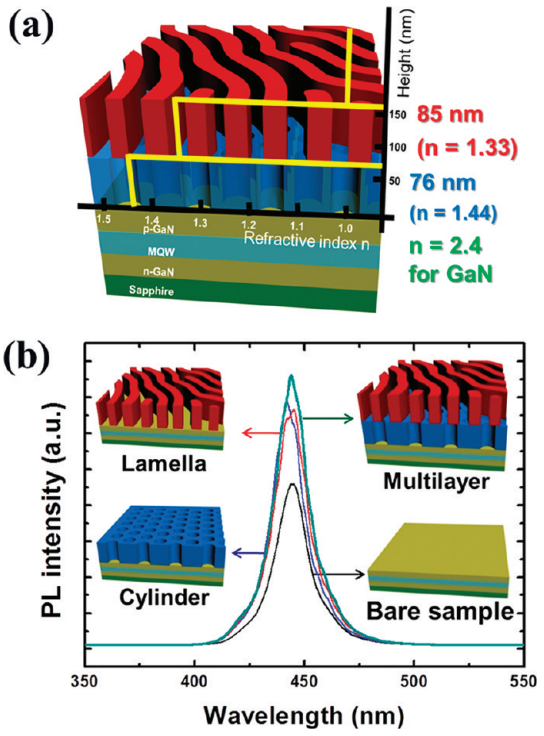

Figure 6. (a) Schematic illustration of BCP multilayers on the GaN LED for enhanced light extraction efficiency. (b) PL spectra from bare GaN LED, GaN LEDs that were coated with cylinder and lamellar single layer, and SMMA104/cylinder multilayer.

can be produced by a solution process using benzocyclobutene (BCB)-based polymer.[42] In this work, a bilayer consisting of (top) porous and (bottom) nonporous BCB layers was prepared by a natural lithography technique using SiO_2 nanospheres. However, this method cannot produce a well-controlled porous layer and is not applicable to a large area.

To address this challenge, the fabrication of GRIN layers by the simple solution assembly of BCP multilayers was investigated. As illustrated in Figure 6a, multilayer films consisting of cylindrical (bottom) and lamellar (top) layers could be prepared on GaN LED surfaces. After removing the PMMA microdomains, the refractive indices of cylindrical and lamellar layers correspond to 1.44 and 1.33, respectively, and thus the refractive indices gradually change from GaN (n = 2.4) to cylinders (n = 1.44) to lamellae (n = 1.33) to air (n = 1). Furthermore, to enhance the light extraction efficiency, the thickness of each layer should satisfy the anti-reflective condition, that is, $\lambda/4n$, where λ is the wavelength of light emitting from InGaN quantum wells (QWs), 440 nm. Accordingly, the thicknesses of cylindrical and lamellar layers were adjusted to 76 and 85 nm, respectively. Photoluminescence (PL) spectra were obtained to compare the light output intensity among four possible samples: bare GaN LED samples, GaN LEDs with either a single layer of cylinder and lamellae nanostructures, and GaN LEDs with a gradient

multilayer structure. As can be seen from Figure 6b, the PL intensity from InGaN QWs was the strongest from the GaN LED multilayer nanostructure through reduction of the Fresnel reflections. In this case, the PL intensity was increased by 67% comparing to bare GaN LED, and by 14 and 11% compared to those with cylindrical and lamellar single layers, respectively. According to Kim *et al.*,[40] a GRIN layer was fabricated with 6 ITO multilayers by the oblique angle deposition technique, and it was observed that the PL intensity of GaN LED with a GRIN layer was increased by 24.3% over LED with an ITO single layer. Considering that the PL intensities were compared between the single layers and the bilayer in our system, we believe that such an increase is not trivial.

CONCLUSIONS

In summary, we have demonstrated the directed formation of complex, 3D multilayered nanostructures from cross-linkable BCPs based on registration of bilayer films through a multilayer process. For a lamellae/cylindrical multilayer configuration, it was observed that the underlying film of PMMA cylinders vertically oriented in a PS matrix can act as a neutral layer, resulting in perpendicular orientation of a lamellae diblock copolymer film. A significant feature of the multilayer structure is that the PMMA lamellae in SMMA104 are in registration with the underlying PMMA cylinders, where the diameter of cylinders is similar to the size of PMMA lamellae. It is postulated that this registration is due to the minimization of unfavorable wetting interactions at the interface of the two block copolymer films. For SMMA42, having smaller size than the diameter of underlying cylinder, we also observed the perpendicular orientation of lamellae on the cross-linked cylinder layers. According to theoretical calculation of interfacial free energy, it was shown that the perpendicular orientation of lamellae in both SMMA104 and SMMA42 can be ascribed to the entropically driven, nematic interactions between polymer chains at the interface. This work demonstrates the orientation and registration between different diblock copolymer morphologies and illustrates the ability to construct complex 3D nanostructures through a multilayer process. These multilayered structures can be used to significantly enhance light extraction in GaN LEDs through the generation of a refractive index gradient with controlled film thicknesses. Further systematic studies to both understand the assembly process and to develop approaches to other 3D nanostructures are in progress.

METHODS

Synthesis of Cross-Linkable BCP, P(*S-r*-S-N_3)-*b*-PMMA. Cross-linkable PS-*b*-PMMA BCP, denoted P(S-*r*-S-N_3)-*b*-PMMA, was synthesized *via* reversible addition−fragmentation transfer (RAFT) polymerization. First, methylmethacrylate (10 g, 99.8 mmol), 2,2′-azobis(2-methylpropionitrile) (AIBN) (4.8 mg, 0.030 mmol), and RAFT agent (90 mg, 0.30 mmol) were mixed and degassed. The reaction was carried out at 80 °C for 5 h. The reaction mixture was then precipitated into methanol, resulting in PMMA-RAFT macroinitiator as a pink powder (M_n = 21 000 g/mol and PDI = 1.20). To add the cross-linkable block, PMMA-RAFT (0.4 g, 0.019 mmol), styrene (9.13 g, 87.7 mmol), 4-vinylbenzyl chloride (0.2 g, 1.31 mmol), and AIBN (0.2 g, 1.22 mmol) were mixed and degassed. The reaction was carried out at 70 °C for 48 h. The reaction mixture was then precipitated into methanol, resulting in P(S-*r*-S-Cl)-*b*-PMMA, **1**, as a pink powder (M_w = 69 000 g/mol and PDI = 1.20). To avoid the coupling reaction during the azidation, the dithioester end group was removed by reaction with AIBN in toluene under nitrogen at 80 °C for 6 h. The solution was precipitated in methanol, yielding a white powder, **2**. The polymer was then mixed with 3 equiv if sodium azide in dimethylformamide, and a mixture was stirred at the room temperature for 24 h. The solution was filtered and precipitated in methanol to obtain a white powder, **3**, as a final product: M_w = 69 000 g/mol and PDI = 1.20; ^{1}H NMR (300 MHz, $CDCl_3$, δ) 0.6−2.6 (m, CH_2, CH, CH_3), 3.20−3.65 (s, OCH_3), 4.10−4.35 (s, $ArCH_2N_3$) and 6.4−7.5 (m, ArH).

Preparation of BCP Thin Films. Two lamellar forming PS-*b*-PMMA BCPs, SMMA104 (M_n = 104 000 g/mol), and SMMA42 (M_n = 42 000 g/mol) were purchased from Polymer Source Inc. To prepare the BCP multilayer films, a silicon wafer was first neutralized using photo-cross-linkable PS-*r*-PMMA random copolymer, P(S-*r*-(S-N_3)-*r*-MMA), that has been reported previously.[21] Thin films of PS-*b*-PMMA BCPs were prepared on these substrates by spin-casting of toluene solutions. The thicknesses were controlled by adjusting the BCP concentration in toluene. Films were annealed at 160 °C (cross-linkable BCP) or 190 °C (SMMA104 and SMMA42) for 24 h. To fabricate the BCP multilayers, the thin films of P(S-*r*-S-N_3)-*b*-PMMA were subsequently cross-linked at 250 °C for 1 h under vacuum. Toluene solutions of SMMA104 or SMMA42 were then spin-coated onto the cross-linked films, resulting in multilayer thin films. The films were then annealed at 190 °C for 24 h. To cleave the PMMA block, the films were irradiated by deep UV light with a wavelength of 254 nm at a dose of 25 J/cm^2 (XX-15S; UVP Inc.) under vacuum for 10 min, rinsed in acetic acid, and then rinsed in water. To prepare GRIN films on the GaN LED, commercial 2 in. GaN-based light-emitting diode (LED) structure with InGaN multi-quantum wells (MQWs) were used as substrates. In this case, it should be noted that the fabrication procedure of BCP films is the same as above.

Characterization of BCP Thin Films. SFM images were obtained in the height mode using a Digital Instruments Multimode scanning force microscope in the tapping mode. Film morphologies were also examined by FE-SEM (Hitachi, S-4300). Samples for TEM were prepared on silicon substrates having a thick layer of silicon oxide. These films were floated onto the surface of a 5 wt % HF solution and then picked up on a Cu grid. A Tecnai 20 electron microscope operating at 200 kV was used to examine the morphology. GISAXS experiments were carried out at the 4C2 beamlines at the Pohang Accelerator Laboratory (PAL), Korea. Two-dimensional GISAXS patterns were recorded using a CCD detector positioned at the end of a vacuum guide tube when the X-rays pass through the BCP thin films under vacuum, where the operating conditions were set to a wavelength of 1.38 Å and a sample-to-detector distance of 2.2 m. To measure the light extraction efficiency of BCP films on the GaN LED, the PL spectra were obtained by using 325 nm wavelength HeCd laser (Kimmon Co.), where the laser power was 2.5 mW.

Theoretical Calculation. We consider a lamellar-forming block copolymer film coated on cross-linked layer of a hexagonal

cylinder. The interlamellar distances of lamellar phase in bulk and in the film bound to cross-linked layer are denoted by L_o and L, respectively, and similarly, the cylinder-to-cylinder distances of a hexagonal cylinder in bulk and in the layer bound to the upper lamellar film are denoted by C_o and C, respectively. The free energy change ΔF per chain of lamellar phase on cross-linked cylinder layer (CCL) is given as $\Delta F = (1 - \phi)\Delta F_{CCL} + \phi\Delta F_{lam}$, where ΔF_{CCL} is the elastic energy change of CCL from its undeformed state, ΔF_{lam} is the free energy change of lamellar film on CCL (deviated from the bulk free energy $F_{lam,o}$), and ϕ is the volume fraction of lamellar film in the whole layer (lamellar film and CCL). In what follows, we express all the free energies F and the length scales X ($X = L, C, C_o$) in units of $F_{lam,o}$ and L_o such that $\Delta\tilde{F} = \Delta F/F_{lam,a}$ and $\tilde{X} = X/L_o$. Using the affine network model the elastic energy change of CCL, ΔF_{CCL} takes the form of

$$\Delta\tilde{F}_{CCL} = \kappa\tilde{C}^2\left[\left(\frac{\tilde{C}_o}{\tilde{C}}\right)^3 - 3\left(\frac{\tilde{C}_o}{\tilde{C}}\right) + 2\right] \quad (1)$$

where κ is the elasticity constant of CCL relating to molecular parameters such as the number of cross-links in the CCL. The free energy change of lamellar film is the sum of the stretching energy of AB diblock chain (let A and B denote PMMA and PS, respectively), the A/B interfacial energy, the lamellar/CCL interfacial energy, and the lamellar/air interfacial energy. Using strong segregation theory, the free energy changes per chain of lamellar film for $L_\perp$ ($\Delta F_{lam,\perp}$) turns out be

$$\Delta\tilde{F}_{lam,\perp} = \frac{2\tilde{P}_{AB}}{3\tilde{a}}\tilde{L} + \frac{1}{6\tilde{a}}\tilde{L}\left[\frac{1}{f^2}\int_{\tilde{V}} A\mathrm{d}\mathbf{r}\tilde{z}^2 + \frac{1}{(1-f)^2}\int_{\tilde{V}} B\mathrm{d}\mathbf{r}\tilde{z}^2\right] + \frac{1}{3\tilde{a}}\gamma_{AB}\left[f\delta + \frac{1}{2}(\sigma - \delta) + \Psi\gamma_{AB} + 2\gamma_{e,\perp} + 2\gamma_{n,\perp}\right] - 1 \quad (2)$$

Here d is the film thickness of lamellar layer, P_{AB} is the perimeter of an A/B interface at the cross section of the lamellar film, f is the composition of the A block in the lamellar layer, V_α indicates an integral over the volume of the α component (α = A or B), and z is the shortest distance from the A/B interface; γ_{AB} is the A/B interfacial tension, $\sigma = \gamma_A + \gamma_B$ and $\delta = \gamma_A - \gamma_B$, where γ_α is the surface tension of component α (α = A, B), and Ψ is the areal fraction of A/B interlayer contacts relative to the total lamellar/cylinder interlayer contacts. The last two terms $\gamma_{e,\perp}$ and $\gamma_{n,\perp}$ in the second bracket are the negative surface tensions arising from the entropic contributions to the surface/polymer interfacial tension for $L_\perp$. The former ($\gamma_{e,\perp}$) is the entropy-originated surface tension due to the chain end effect, which reflects the tendency of chain ends migrating toward the boundary of the film (the chain ends undergo relatively less (configurational) entropic loss than midsegments). The last term ($\gamma_{n,\perp}$) arises from *nematic interaction* attributed to the surface preferring chain segments to lie along the surface. The free energy change per chain for $L_\parallel$, on the other hand, is given as

$$\Delta\tilde{F}_{lam,\parallel} = \frac{\nu}{3\tilde{a}} + \frac{4\tilde{a}^2}{3\nu^2} + \frac{1}{3\tilde{a}}\gamma_{AB}\left[\frac{1}{2}(\sigma - (-1)^\nu\delta) + g\gamma_{AB} + 2\gamma_{e,\parallel}\right] - 1 \quad (3)$$

where ν is the number of A/B interfaces in the lamellar film, g is the composition of the A block in the CCL, and $\gamma_{e,\parallel}$ is the contribution of chain end effect to the surface tension for $L_\parallel$. Minimization of $\Delta F_\perp = (1 - \phi)\Delta F_{CCL} + \phi\Delta F_{lam,\perp}$ with respect to L and C gives the free energy change per chain for $L_\perp$ on CCL. Similarly, the free energy change per chain for $L_\parallel$ on CCL is given by minimizing $\Delta F_\parallel = (1 - \phi)\Delta F_{CCL} + \phi\Delta F_{lam,\parallel}$ with respect to ν.

Acknowledgment. This work was supported by National Research Foundation of Korea Grant funded by the Korean Government (MOEHRD) (2010-0015294, 2010-0016304, 2010-0027751). D.Y.R. acknowledges Converging Research Center Program (2010K001430) and APCPI ERC program (R11-2007-050-00000), which are funded by the Ministry of Education, Science & Technology (MEST), Korea. C.J.H. acknowledges support from the Semiconductor Research Corporation (SRC) and its Focus Center Research Program (FCRP)—Center for Functional Engineered NanoArchitectonics (FENA) as well as the UCSB Materials Research Laboratory (NSF Grant DMR05-20415).

Supporting Information Available: Size exclusion chromatography traces of P(S-*r*-S-N_3)-*b*-PMMA BCP and additional SFM, GISAXS, and SEM images. This material is available free of charge *via* the Internet at http://pubs.acs.org.

REFERENCES AND NOTES

1. Hawker, C. J.; Russell, T. P. Block Copolymer Lithography: Merging "Bottom-Up" with "Top-Down" Processes. *MRS Bull.* **2005**, *30*, 952–966.
2. Bang, J.; Jeong, U.; Ryu, D. Y.; Russell, T. P.; Hawker, C. J. Block Copolymer Nanolithography: Translation of Molecular Level Control to Nanoscale Patterns. *Adv. Mater.* **2009**, *47*, 4769–4792.
3. Fasolka, M. J.; Mayes, A. M. Block Copolymer Thin Films: Physics and Applications. *Annu. Rev. Mater. Res.* **2001**, *31*, 323–355.
4. Segalman, R. A. Patterning with Block Copolymer Thin Films. *Mater. Sci. Eng. R* **2005**, *48*, 191–226.
5. Black, C. T.; Ruiz, R.; Breyta, G.; Cheng, J. Y.; Colburn, M. E.; Guarini, K. W.; Kim, H. C.; Zhang, Y. Polymer Self Assembly in Semiconductor Microelectronics. *IBM J. Res. Dev.* **2007**, *51*, 605–633.
6. Cheng, J. Y.; Ross, C. A.; Smith, H. I.; Thomas, E. L. Templated Self-Assembly of Block Copolymers: Top-Down Helps Bottom-Up. *Adv. Mater.* **2006**, *18*, 2505–2521.
7. Kim, J. K.; Lee, J. I.; Lee, D. H. Self-Assembled Block Copolymers: Bulk to Thin Film. *Macromol. Res.* **2008**, *16*, 267–292.
8. IBM Brings Nature to Computer Chip Manufacturing, *Am. Ceram. Soc. Bull.*, May 3, 2007.
9. Kim, S. O.; Solak, H. H.; Stoykovich, M. P.; Ferrier, N. J.; de Pablo, J. J.; Nealey, P. F. Epitaxial Self-Assembly of Block Copolymers on Lithographically Defined Nanopatterned Substrates. *Nature* **2003**, *424*, 411–414.
10. Edwards, E. W.; Montague, M. F.; Solak, H. H.; Hawker, C. J.; Nealey, P. F. Precise Control over Molecular Dimensions of Block-Copolymer Domains Using the Interfacial Eenergy of Chemically Nanopatterned Substrates. *Adv. Mater.* **2004**, *16*, 1315–1319.
11. Stoykovich, M. P.; Kang, H.; Daoulas, K. C.; Liu, G.; Liu, C.-C.; de Pablo, J. J.; Mueller, M.; Nealey, P. F. Directed Self-Assembly of Block Copolymers for Nanolithography: Fabrication of Isolated Features and Essential Integrated Circuit Geometries. *ACS Nano* **2007**, *1*, 168–175.
12. Stoykovich, M. P.; Mueller, M.; Kim, S. O.; Solak, H. H.; Edwards, E. W.; de Pablo, J. J.; Nealey, P. F. Directed Assembly of Block Copolymer Blends into Nonregular Device-Oriented Structures. *Science* **2005**, *308*, 1442–1446.
13. Ruiz, R.; Kang, H. M.; Detcheverry, F. A.; Dobisz, E.; Kercher, D. S.; Albrecht, T. R.; de Pablo, J. J.; Nealey, P. F. Density Multiplication and Improved Lithography by Directed Block Copolymer Assembly. *Science* **2008**, *321*, 936–939.
14. Cheng, J. Y.; Rettner, C. T.; Sanders, D. P.; Kim, H. C.; Hinsberg, W. D. Dense Self-Assembly on Sparse Chemical Patterns: Rectifying and Multiplying Lithographic Patterns Using Block Copolymers. *Adv. Mater.* **2008**, *20*, 3155–3158.
15. Daoulas, K. C.; Muller, M.; Stoykovich, M. P.; Park, S.-M.; Papakonstantopoulos, Y. J.; de Pablo, J. J.; Nealey, P. F.; Solak, H. H. Fabrication of Complex Three-Dimensional Nanostructures from Self-Assembling Block Copolymer Materials on Two-Dimensional Chemically Patterned Templates with Mismatched Symmetry. *Phys. Rev. Lett.* **2006**, *96*, 036104/1–036104/4.
16. Lee, S.; Lee, B.; Kim, B. J.; Park, J.; Yoo, M.; Bae, W. K.; Char, K.; Hawker, C. J.; Bang, J.; Cho, J. H. Free-Standing Nanocomposite Multilayers with Various Length Scales, Adjustable Internal Structures, and Functionalities. *J. Am. Chem. Soc.* **2009**, *131*, 2579–2587.
17. Kim, E.; Shin, C.; Ahn, H.; Ryu, D. Y.; Bang, J.; Hawker, C. J.; Russell, T. P. Size Control and Registration of Nano-structured Thin Films by Cross-Linkable Units. *Soft Matter* **2008**, *4*, 475–479.

18. Ruiz, R.; Sandstrom, R. L.; Black, C. T. Induced Orientational Order in Symmetric Diblock Copolymer Thin Films. *Adv. Mater.* **2007**, *19*, 587–591.
19. Rose, F.; Bosworth, J. K.; Dobisz, E. A.; Ruiz, R. Three-Dimensional Mesoporous Structures Fabricated by Independent Stacking of Self-Assembled Films on Suspended Membranes. *Nanotechnology* **2011**, *22*, 035603/1–035603/7.
20. Drockenmuller, E.; Li, L. Y. T.; Ryu, D. Y.; Harth, E.; Russell, T. P.; Kim, H.-C.; Hawker, C. J. Covalent Stabilization of Nanostructures: Robust Block Copolymer Templates from Novel Thermoreactive Systems. *J. Polym. Sci., Part A: Polym. Chem.* **2005**, *43*, 1028–1037.
21. Bang, J.; Bae, J.; Lowenhielm, P.; Spiessberger, C.; Given-Beck, S. A.; Russell, T. P.; Hawker, C. J. Facile Routes to Patterned Surface Neutralization Layers for Block Copolymer Lithography. *Adv. Mater.* **2007**, *19*, 4552–4557.
22. Mansky, P.; Liu, Y.; Huang, E.; Russell, T. P.; Hawker, C. Controlling Polymer−Surface Interactions with Random Copolymer Brushes. *Science* **1997**, *275*, 1458–1460.
23. Mansky, P.; Russell, T. P.; Hawker, C. J.; Pitsikalis, M.; Mays, J. Ordered Diblock Copolymer Films on Random Copolymer Brushes. *Macromolecules* **1997**, *30*, 6810–6813.
24. Ryu, D. Y.; Shin, K.; Drockenmuller, E.; Hawker, C. J.; Russell, T. P. A Generalized Approach to the Modification of Solid Surfaces. *Science* **2005**, *308*, 236–239.
25. Ryu, D. Y.; Wang, J. Y.; Lavery, K. A.; Drockenmuller, E.; Satija, S. K.; Hawker, C. J.; Russell, T. P. Surface Modification with Cross-Linked Random Copolymers: Minimum Effective Thickness. *Macromolecules* **2007**, *40*, 4296–4300.
26. Ham, S.; Shin, C.; Kim, E.; Ryu, D. Y.; Jeong, U.; Russell, T. P.; Hawker, C. J. Microdomain Orientation of PS-*b*-PMMA by Controlled Interfacial Interactions. *Macromolecules* **2008**, *41*, 6431–6437.
27. Ryu, D. Y.; Ham, S.; Kim, E.; Jeong, U.; Hawker, C. J.; Russell, T. P. Cylindrical Microdomain Orientation of PS-*b*-PMMA on the Balanced Interfacial Interactions: Composition Effect of Block Copolymers. *Macromolecules* **2009**, *42*, 4902–4906.
28. Jeong, U.; Kim, H.-C.; Rodriguez, R. L.; Tsai, I. Y.; Stafford, C. M.; Kim, J. K.; Hawker, C. J.; Russell, T. P. Asymmetric Block Copolymers with Homopolymers: Routes to Multiple Length Scale Nanostructures. *Adv. Mater.* **2002**, *14*, 274–276.
29. Fredrickson, G. H. Surface Ordering Phenomena in Block Copolymer Melts. *Macromolecules* **1987**, *20*, 2535–2542.
30. Pickett, G. T.; Witten, T. A.; Nagel, S. R. Equilibrium Surface Orientation of Lamellae. *Macromolecules* **1993**, *26*, 3194–3199.
31. Busch, P.; Posselt, D.; Smilgies, D. M.; Rheinlander, B.; Kremer, F.; Papadakis, C. M. Lamellar Diblock Copolymer Thin Films Investigated by Tapping Mode Atomic Force Microscopy: Molar-Mass Dependence of Surface Ordering. *Macromolecules* **2003**, *36*, 8717–8727.
32. Bollinne, C.; Stone, V. W.; Carlier, V.; Jonas, A. M. Density Perturbations in Polymers Near a Solid Substrate: An X-ray Reflectivity Study. *Macromolecules* **1999**, *32*, 4719–4724.
33. van der Lee, A.; Hamon, L.; Holl, Y.; Grohens, Y. Density Profiles in Thin PMMA Supported Films Investigated by X-ray Reflectometry. *Langmuir* **2001**, *17*, 7664–7669.
34. Wang, R.; Chen, Y. L.; Hu, J. L.; Xue, G. Depletion-Induced Surface Alignment of Asymmetric Diblock Copolymer in Selective Solvents. *J. Chem. Phys.* **2008**, *129*, 044907/1–044907/8.
35. Xu, Y.; Feng, J.; Zhang, Z.; Wang, Y.; Chen, J.; Zhu, X. Depletion Phenomenon in Diblock Copolymer Films: A Dissipative Particle Dynamics Simulation. *Mol. Simul.* **2010**, *36*, 468–473.
36. Fasolka, M. J.; Harris, D. J.; Mayes, A. M.; Yoon, M.; Mochrie, S. G. J. Observed Substrate Topography-Mediated Lateral Patterning of Diblock Copolymer Films. *Phys. Rev. Lett.* **1997**, *79*, 3018–3021.
37. Sivaniah, E.; Hayashi, Y.; Matsubara, S.; Kiyono, S.; Hashimoto, T.; Fukunaga, K.; Kramer, E. J.; Mates, T. Symmetric Diblock Copolymer Thin Films on Rough Substrates. Kinetics and Structure Formation in Pure Block Copolymer Thin Films. *Macromolecules* **2005**, *38*, 1837–1849.
38. Truong, T. A.; Campos, L. M.; Matioli, E.; Meinel, I.; Hawker, C. J.; Weisbuch, C.; Petroff, P. M. Light Extraction from GaN-Based Light Emitting Diode Structures with a Noninvasive Two-Dimensional Photonic Crystal. *Appl. Phys. Lett.* **2009**, *94*, 023101/1–023101/3.
39. Xi, J. Q.; Schubert, M. F.; Kim, J. K.; Schubert, E. F.; Chen, M. F.; Lin, S. Y.; Liu, W.; Smart, J. A. Optical Thin-Film Materials with Low Refractive Index for Broadband Elimination of Fresnel Reflection. *Nat. Photonics* **2007**, *1*, 176–179.
40. Kim, J. K.; Chhajed, S.; Schubert, M. F.; Schubert, E. F.; Fischer, A. J.; Crawford, M. H.; Cho, J.; Kim, H.; Sone, C. Light-Extraction Enhancement of GaInN Light-Emitting Diodes by Graded-Refractive-Index Indium Tin Oxide Anti-reflection Contact. *Adv. Mater.* **2008**, *20*, 801–804.
41. Liu, D. S.; Lin, T. W.; Huang, B. W.; Juang, F. S.; Lei, P. H.; Hu, C. Z. Light-Extraction Enhancement in GaN-Based Light-Emitting Diodes Using Grade-Refractive-Index Amorphous Titanium Oxide Films with Porous Structures. *Appl. Phys. Lett.* **2009**, *94*, 143502/1–143502/3.
42. Kim, B. J.; Bang, J.; Kim, S. H.; Kim, J. Enhancement of the Light-Extraction Efficiency of GaN-Based Light Emitting Diodes Using Graded-Refractive-Index Layer by SiO_2 Nanosphere Lithography. *J. Electrochem. Soc.* **2010**, *157*, H449–H451.